2020 IEEE International Conference on Robotics and Automation (ICRA)
31 May - 31 August, 2020. Paris, France

Design and Kinematic Modeling of a Novel Steerable Needle for Image-Guided Insertion

Yuyang Chen, Haozhe Yang, Xu Liu and Kai Xu*, *Member, IEEE*

***Abstract*—Needle-based procedures, such as biopsy and percutaneous tumor ablation, highly depend on the accuracy of needle placement. The accuracy is significantly affected by the needle-tissue interaction no matter what needles (straight or steerable) are used. Due to the unknown tissue mechanics, it is challenging to achieve high accuracy in practice. This paper hence proposes a needle design with an articulated tip for increased steerability and improved needle path consistency. Due to the passive needle tip articulation, tissue mechanics always plays a dominant role such that the needle creates similar paths with approximately piece-wise constant curvature in different tissues. Kinematics model for the proposed needle is presented. The algorithms of path planning and needle tip pose estimation under external imaging modality are developed. Experimental verifications were conducted to demonstrate the needle's steerability as well as the target-reaching capability with obstacles avoidance.**

I. Introduction

As an effective means of diagnosis and treatment, needle is frequently used in biopsy, brachytherapy and ablation. However, challenges are often encountered while using a stiff needle. For example, the needle may deviate from its straight insertion path due to a non-uniform tissue-needle interaction. The lack of ability to avoid obstacles also makes it difficult to reach specific targets.

Over the past decades, varieties of approaches that achieve controlled needle steering have been proposed [1, 2], mainly including i) base manipulation [3-5], ii) asymmetric tip [6-9], and iii) active cannula [10-13].

In the approach of base manipulation, the needle behaves like a beam supported at the insertion port. The steerability significantly decreases as the needle is inserted deeper into the tissue [14].

The approach with asymmetric tips is probably the most widely applied, where the needle is deflected by the asymmetric force produced by the needle-tissue interaction. Quantities of works have been done to improve the needle's steerability, either by i) reducing the bending stiffness of the needle, such as using notched flexible needle shafts [15], or ii) by increasing the steering forces, including the use of flexure-based tips [7], pre-curved or kinked tips [16, 17], and actuated tips [8, 9, 18].

Active cannulae have been utilized as steerable needles from a concentric telescoped configuration. It possibly shows a higher level of steerability due to its pre-curved shapes. However, the needle placement accuracy is further complicated by the interaction between the pre-curved concentric needle tubes [12, 13].

Placement accuracy of the aforementioned steerable needles heavily depends on the tissue-needle interaction. Besides the non-holonomic kinematics model to describe a needle's 6-DoFs (Degrees of Freedom) motions [6], mechanics-based models were also developed to incorporate the deformations of both the needle and the surrounding tissues [18-20]. Nevertheless, uncertainty in the tissues' mechanical parameters makes it challenging to achieve accurate needle placement.

To improve steerability and to reduce the influence from tissues with different mechanical properties, a novel bevel tip flexible needle with a passively articulated tip segment and a notched stem segment is proposed in this paper. As shown in Fig. 1, the needle's tip segment is composed of several rigid links cut from a stainless steel tube. Each link can rotate freely within a small range with respect to its adjacent links. The needle's stem segment possesses a notched pattern for increased flexibility.

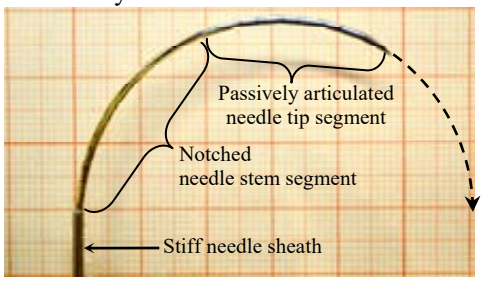

Fig. 1. The proposed needle steers in tissue simulant. The multiple articulations in the needle's tip segment help form and maintain the needle's tight path curvature.

Because the articulation in the needle's tip segment is passive, the lateral force generated by the tip bevel can easily deflect the needle to the joint limits to realize designed curvature during needle insertion. In contrast to the existing needle designs whose bending depends on the tissue-needle

Manuscript received September 15, 2019. This work was supported in part by the National Natural Science Foundation of China (Grant No. 51722507, Grant No. 51435010 and Grant No. 91648103), and in part by National Key R&D Program of China (Grant No. 2017YFC0110800).

Yuyang Chen is with the RII Lab (Lab of Robotics Innovation and Intervention), UM-SJTU Joint Institute, Shanghai Jiao Tong University, Shanghai, 200240, China (email: supandoria@sjtu.edu.cn).

Haozhe Yang, Xu Liu and Kai Xu are with the State Key Laboratory of Mechanical System and Vibration, School of Mechanical Engineering, Shanghai Jiao Tong University, Shanghai, 200240, China (asterisk indicates the corresponding author, emails: silence1004@sjtu.edu.cn, xu.liu@sjtu.edu.cn and k.xu@sjtu.edu.cn).

interaction on a higher level, the realized steering curvature may vary within different tissues. Due to the passive articulation of the proposed needle's tip segment, it is expected to achieve similar and consistent path curvature in different tissues.

To reach a target while avoiding interfering with obstacles, path planning strategies shall be implemented on top of the needle motion models. Adopted path planning approaches include the uses of a potential field [3], a stochastic model [21], a RRT (Rapidly explored Random Tree) algorithm [22], and the inverse kinematics for piecewise constant-curvature needle paths [23]. In this paper, an approach similar to the latter one is put forward. The path planning and obstacle avoidance is solved via the inverse kinematics based on experimentally verified needle path curvature. To compensate the un-modeled behaviors of the passive needle tip segment and the tissue, the paths were repeatedly re-planned based on the estimated pose of the needle tip from an external imaging modality. Planar needle insertion experiments were conducted.

This paper is organized as follows. The working principle of the proposed needle is explained in Section II. Design specifications are discussed in Section III. Then a model-based path planning algorithm is presented in Section IV. In Section V, experimental validations are reported and the results are discussed. Finally, the conclusions and future works are summarized in Section VI.

II. Working Principle

The proposed needle is expected to generate and maintain a tight curvature in different tissues, due to its passive articulation tip design. As shown in Fig. 2, the proposed needle is composed of two parts: the *needle tip segment* and the *needle stem segment*.

The function of the needle tip segment is to create a steered path. It consists of several rigid links with hinged joints cut from a stainless steel tube. Two adjacent hinges are arranged orthogonally so that the needle tip segment bends freely in different directions. This feature also enables the needle's axial rotation while being in a curved path.

A bevel tip is added to the end of the distal link. While inserted into a tissue, the bevel tip generates asymmetric forces that cause the hinges to rotate to their limits. The shape of the needle tip segment approximates an arc with constant curvature. Since the needle tip segment is kept at its maximally deflected shape in response to different levels of steering forces, this helps the needle to follow paths with similar curvature in different tissues.

The needle stem segment is designed to transmit insertion forces and axial torsions. The needle stem should also be flexible enough to follow the path created by the needle tip segment. Therefore, equidistantly distributed notches in different directions are cut on the stem. The notches reduce the bending stiffness of the stem while maintaining a relatively high torsional rigidity.

To reach a target while avoiding obstacles, the needle is controlled by an axial rotation and an insertion, thus creating a path with multiple constant curvature arcs, as referred to Fig. 2-(b). The design considerations for the needle to steer with a prescribed curvature will be elaborated in Section III. And the planning of such piecewise constant curvature paths with the kinematics model is detailed in Section IV.

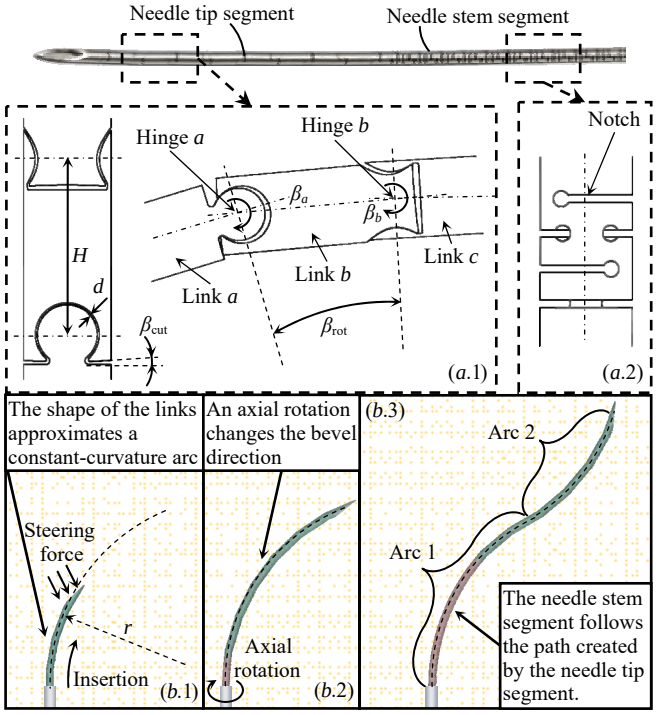

Fig. 2. The working principle of the proposed needle: (a) detailed geometry of the needle tip segment and the needle stem segment; (b) process of the needle following a path of two constant-curvature arcs.

III. Needle Design

The proposed needle can be manufactured by cutting the designed geometric patterns on the surface of a stainless steel tube via laser cutting. The stainless-steel tube has an outer diameter of 1.2 mm and an inner diameter of 0.7 mm, which is close to an 18-gauge needle. The geometric parameters of these cuts are shown in Fig. 2-(a) and listed in Table I.

TABLE I
Needle Design Variables

Symbol	Definition	Values
D_o D_i	Outer and inner diameters of the needle.	1.2 mm 0.7 mm
H	Length of the links in the needle tip segment.	3 mm
d	Width of the clearance created by laser machining.	0.025 mm
r	Designed steering radius of the needle.	30 mm
β_{cut}	Cutting inclination angle of the hinge in the needle tip segment.	4.13°
β_{rot}	Allowable rotating angle contributed by two adjacent hinges.	11.46°
E	Young's modulus of the needle's material.	190 GPa

A small radius of curvature improves the needle's ability in reaching targets and avoiding obstacles in confined spaces. For example, the radius of curvature shall be less than 50 mm for the radiofrequency ablation of liver tumors [17]. In this

paper, the design goal radius of curvature is set to $r = 30$ mm. As referred to Fig. 2-(*a*), the bending curvature radius of the needle tip segment is calculated using Eq. (1). The goal radius gives an allowable rotating angle of 11.46°.

$$r = 2H / \beta_{\text{rot}} \tag{1}$$

Since the laser machine creates a clearance in the hinges with a width d, the allowable rotations between the links are increased and this cannot be ignored. As a result, β_{rot} is contributed by the rotations of both Hinge *a* and Hinge *b*, as formulated in Eq. (2).

$$\beta_{\text{rot}} = \beta_a + \beta_b \tag{2}$$

Where β_a and β_b are the rotation angles of Hinge *a* and Hinge *b*.

To obtain the relationship between β_{rot} and the cutting inclination angle β_{cut} under a laser cutting clearance width d, each link is virtually perturbed in the plane shown in Fig. 2-(a) (i.e., 2-DoF translation and 1-DoF rotation). The allowable rotating β_a and β_b values were found using the genetic method function *ga* in Matlab (the MathWorks Inc.) under the contour interference constraints with the planar perturbations.

The β_{rot} values with respect to a grid of d and β_{cut} for the proposed needle were obtained. As shown in Fig. 3, these values were fitted into a plane in Eq. (3) with an RMSE (Root-Mean-Square Error) of 0.1608 degrees.

$$\beta_{\text{rot}} = 1.09\beta_{\text{cut}} + 296d - 0.433 \tag{3}$$

The laser cutting clearance width d was found approximately 0.025 mm by adjusting the power and focus of the laser. The cutting inclination angle β_{cut} was then determined from β_{actual} that corresponded to the objective bending radius of curvature $r = 30$ mm by Eq. (1) and Eq. (3).

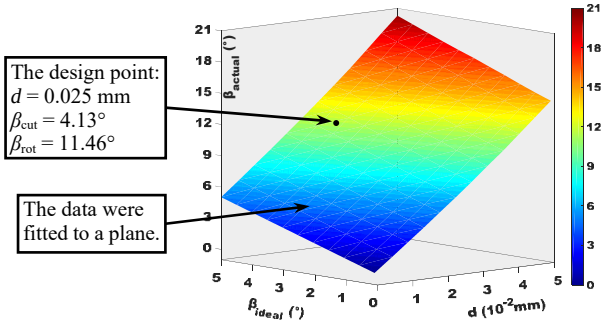

Fig. 3. The data of the allowable rotating angle β_{rot} found via a generic method

IV. Model-Based Path Planning

In this section, the path planning algorithm based on the kinematics model of the proposed needle is first introduced. A framework of the needle tip pose estimation and path re-planning is then presented.

A. Forward Kinematics

For the purpose of proof of concept, the needle's insertion and axial rotation are performed separately in the presented study. This gives a path composed of several arcs with constant curvature. Before developing the kinematics model, several coordinates and the configuration parameters of the arcs are defined, referring to Fig. 4.

- *World coordinate* $\{w\} = \{\mathbf{x}_w, \mathbf{y}_w, \mathbf{z}_w\}$, is a fixed and known reference frame.
- *Arc base coordinate* $\{ib\} = \{\mathbf{x}_{ib}, \mathbf{y}_{ib}, \mathbf{z}_{ib}\}$, is attached to the start point of i^{th} ($i = 1, 2, 3, \ldots, n$) arc. $\mathbf{z}_{ib}$ is axially aligned with the needle insertion direction, and $\mathbf{y}_{ib}$ is pointing outwards from the center of the $(i–1)^{\text{th}}$ arc.
- *Arc bending coordinate* $\{ic\} = \{\mathbf{x}_{ic}, \mathbf{y}_{ic}, \mathbf{z}_{ic}\}$, is obtained by a right-handed rotation of $\{ib\}$ about $\mathbf{z}_{ib}$ by an angle δ_i.
- *Arc tip coordinate* $\{ie\} = \{\mathbf{x}_{ie}, \mathbf{y}_{ie}, \mathbf{z}_{ie}\}$, is obtained by a translation of $\{ic\}$ to the end point of the i^{th} arc, and a right-handed rotation about $\mathbf{x}_{ic}$ by an angle θ_i. $\{ie\}$ coincides with $\{(i+1)b\}$.

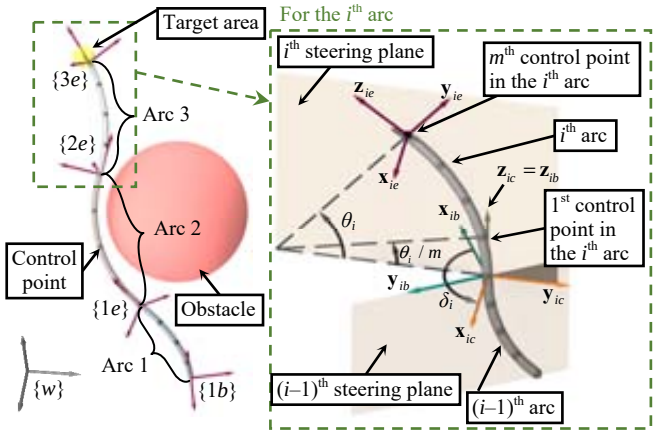

Fig. 4. Coordinate definitions for the needle's forward kinematics

The shape of the entire needle is determined by the configuration vector $\boldsymbol{\psi} = \begin{bmatrix} \boldsymbol{\psi}_1^T & \cdots & \boldsymbol{\psi}_n^T \end{bmatrix}^T$, where $\boldsymbol{\psi}_i = [\theta_i \ \delta_i]^T$ is the configuration vector for the i^{th} circular arc. The steering direction angle δ_i is controlled by the axial rotation input of the needle, and the steering angle θ_i is controlled by the insertion length L_i.

$$\theta_i = L_i / r \tag{4}$$

The position and orientation of $\{ie\}$ with respect to $\{ib\}$ are given as follows.

$${}^{ib}\mathbf{p}_{ie} = r\begin{bmatrix} \sin\delta_i(1-\cos\theta_i) & \cos\delta_i(\cos\theta_i - 1) & \sin\theta_i \end{bmatrix}^T \tag{5}$$

$${}^{ib}\mathbf{R}_{ie} = e^{(\delta_i \mathbf{e}_3)^\wedge} e^{(\theta_i \mathbf{e}_1)^\wedge} \tag{6}$$

Where $\mathbf{e}_1 = [1\ 0\ 0]^T$, $\mathbf{e}_2 = [0\ 1\ 0]^T$ and $\mathbf{e}_3 = [0\ 0\ 1]^T$ are unit Euclidean basis, and the operator $(\bullet)^\wedge$ converses an element in $\mathbb{R}^3$ to its corresponding element in $\mathfrak{so}(3)$.

The pose of the frame at the end of the path $\{ne\}$ with respect to $\{1b\}$ can be calculated in a recursive way as given by Eqs. (7) and (8).

$${}^{1b}\mathbf{p}_{ne} = {}^{1b}\mathbf{R}_{nb}\,{}^{nb}\mathbf{p}_{ne} + {}^{1b}\mathbf{p}_{nb} \tag{7}$$

$${}^{1b}\mathbf{R}_{ne} = {}^{1b}\mathbf{R}_{nb}\,{}^{nb}\mathbf{R}_{ne} \tag{8}$$

The instantaneous kinematics for the i^{th} arc is described by the Jacobians $\mathbf{J}_{vi}$ that map from the configuration velocity to the linear velocity of the arc tip.

$$\mathbf{J}_{\mathbf{v}i} = r\begin{bmatrix} \sin\delta_i \sin\theta_i & \cos\delta_i(1-\cos\theta_i) \\ -\cos\delta_i \sin\theta_i & \sin\delta_i(1-\cos\theta_i) \\ \cos\theta_i & 0 \end{bmatrix} \quad (9)$$

The linear velocity Jacobian for the stacked arcs $\mathbf{J}_{\mathbf{v}}$, is hence formulated as in Eq. (10).

$$\mathbf{J}_{\mathbf{v}} = \begin{bmatrix} \mathbf{\Lambda}_1 & \cdots & \mathbf{\Lambda}_i & \cdots & \mathbf{\Lambda}_n \end{bmatrix},$$
$$\mathbf{\Lambda}_i = {}^{1b}\mathbf{R}_{ib}\left(\mathbf{J}_{\mathbf{v}i} - \left({}^{ib}\mathbf{R}_{ie}\,{}^{ie}\mathbf{p}_{ne}\right)^{\wedge}\mathbf{J}_{\boldsymbol{\omega}i}\right) \quad (10)$$
$$\mathbf{J}_{\boldsymbol{\omega}i} = \begin{bmatrix} \cos\delta_i & 0 \\ \sin\delta_i & 0 \\ 0 & 1 \end{bmatrix}$$

B. Path Planning

Since the needle assumes follow-the-leader motion in the tissue, the path of the needle can be represented by its shape $\boldsymbol{\psi}$, and hence the path planning is achieved by solving the inverse kinematics.

The flowchart of the path planning algorithm can be referred to Fig. 5. The input of the algorithm includes the target position ${}^{w}\mathbf{p}_g$, the obstacle position ${}^{w}\mathbf{p}_o$ and the obstacle radius ρ_o, and the current pose of $\{1b\}$ (${}^{w}\mathbf{p}_{1b}$ and ${}^{w}\mathbf{R}_{1b}$) from which the needle starts. The planning starts by assuming a single-arc configuration (n = 1) and increases n by one if it fails to find a path within the maximum iteration number N_{iter}.

Given the number of arcs n, the resolved motion rate control method [24] is employed to find a feasible path iteratively from an initial configuration $\boldsymbol{\psi} = \mathbf{0}_{2n\times 1}$. Successful path planning is identified if the distance from the needle tip $\{ne\}$ to the target is within a tolerance ε and the path does not interfere with the obstacle. The planning exits if a feasible path is found or the maximum arc number N_{arc} is reached.

The velocity of the needle tip $\{ne\}$ towards the target is measured by the position error between them.

$${}^{1b}\mathbf{v}_{ne} = {}^{1b}\mathbf{e}_{g,ne} = {}^{w}\mathbf{R}_{1b}^{T}\,{}^{w}\mathbf{p}_g - {}^{1b}\mathbf{p}_{ne} \quad (11)$$

To avoid obstacles, a set of control points along the needle path, are selected to detect the interference of the needle path with the obstacles, as demonstrated in Fig. 4. For the i^{th} arc, m control points are equidistantly distributed along the curve, and their positions ${}^{1b}\mathbf{p}_{a\_ij}$ (j = 1, 2, 3, …, m) is formulated as follows.

$${}^{1b}\mathbf{p}_{a\_ij} = {}^{1b}\mathbf{R}_{ib}\, r\begin{bmatrix} \sin\delta_i\left(1-\cos\left(\frac{j}{m}\theta_i\right)\right) \\ \cos\delta_i\left(\cos\left(\frac{j}{m}\theta_i\right)-1\right) \\ \sin\left(\frac{j}{m}\theta_i\right) \end{bmatrix} + {}^{1b}\mathbf{p}_{ib} \quad (12)$$

Assuming the obstacle is represented by a sphere with the center position ${}^{w}\mathbf{p}_o$ and a radius ρ_o, the velocities of the control points are given by Eq. (13).

$${}^{1b}\mathbf{v}_{a\_ij} = \begin{cases} -\dfrac{{}^{1b}\mathbf{e}_{o,a\_ij}}{\left\|{}^{1b}\mathbf{e}_{o,a\_ij}\right\|^2} & \left\|{}^{1b}\mathbf{e}_{o,a\_ij}\right\| < \rho_o \\ 0 & \left\|{}^{1b}\mathbf{e}_{o,a\_ij}\right\| \geq \rho_o \end{cases}, \quad (13)$$
$${}^{1b}\mathbf{e}_{o,a\_ij} = {}^{w}\mathbf{R}_{1b}^{T}\,{}^{w}\mathbf{p}_o - {}^{1b}\mathbf{p}_{a\_ij}$$

The configuration update is then calculated by Eq. (14).

$$\dot{\boldsymbol{\psi}} = \eta_e \mathbf{J}_{\mathbf{v}}^{+}\,{}^{1b}\mathbf{v}_{ne} + \left(\mathbf{I} - \mathbf{J}_{\mathbf{v}}^{+}\mathbf{J}_{\mathbf{v}}\right)\sum_{i=1}^{n}\sum_{j=1}^{m}\eta_{a\_ij}\mathbf{J}_{a\_ij}^{+}\,{}^{1b}\mathbf{v}_{a\_ij} \quad (14)$$

Where $\mathbf{J}^{+} = \mathbf{J}^{T}(\mathbf{J}\mathbf{J}^{T})^{-1}$ is the right pseudo-inverse of $\mathbf{J}$; $\mathbf{J}_{a\_ij}$ is the linear velocity Jacobian for the j^{th} control point on the i^{th} arc; η_e and η_{a_ij} are scaling parameters for velocities ${}^{1b}\mathbf{v}_{ne}$ and ${}^{1b}\mathbf{v}_{a\_ij}$. The use of the null space projector $(\mathbf{I} - \mathbf{J}_{\mathbf{v}}^{+}\mathbf{J}_{\mathbf{v}})$ prioritizes the target-reaching task over the obstacle avoidance. The Jacobian $\mathbf{J}_{a\_ij}$ is determined by the first $2i$ elements of the configuration vector $\boldsymbol{\psi}$.

$$\mathbf{J}_{a\_ij} = \begin{bmatrix} \bar{\mathbf{\Lambda}}_1 & \cdots & \bar{\mathbf{\Lambda}}_k & \cdots & \bar{\mathbf{\Lambda}}_i & \mathbf{0}_{3\times 2(n-i)} \end{bmatrix} \quad (15)$$

Where $\bar{\mathbf{\Lambda}}_k = {}^{1b}\mathbf{R}_{kb}\left(\mathbf{J}_{\mathbf{v}k} - \left({}^{kb}\mathbf{R}_{ke}\,{}^{ke}\mathbf{p}_{a\_ij}\right)^{\wedge}\mathbf{J}_{\boldsymbol{\omega}k}\right)$.

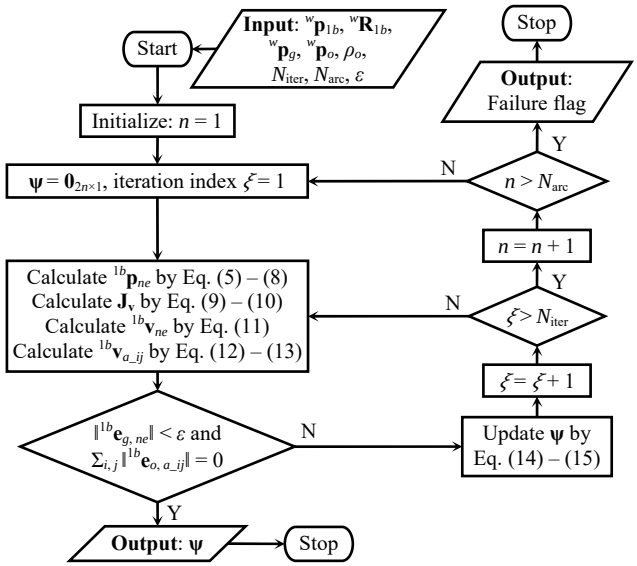

Fig. 5. Flowchart of the path planning algorithm.

C. Needle Tip Pose Estimation

In practice, the needle will not follow the kinematics model perfectly. Unexpected disturbances can prevent the needle from the tracking the path. For example, the needle will fail to steer when traveling through cavities. Un-modeled kinematic factors such as the backlashes in the clearances of the needle tip hinges also decrease the tracking accuracy.

To overcome these drawbacks, the path planning is repeatedly performed based on the current pose of the needle tip. By measuring the tip positions from the imaging modality, the needle tip pose is estimated using an EKF (extended Kalman filter). Since the re-planned path of the needle starts from the current needle tip pose, $\{1b\}$ is set coincident with the current needle tip pose as the input of the path planning algorithm.

For clarity of the expressions, the current needle tip position and orientation with respect to $\{w\}$ is represented by $\mathbf{p}_t$ and $\mathbf{R}_t$ respectively, where t = 1, 2, 3, …, is the discrete time index.

To develop the kinematics model that accounts for the needle's motion uncertainties, the needle tip's orientation is also parameterized by Euler angles $\boldsymbol{\varphi}_t = [\varphi_{\mathbf{x},t}\ \varphi_{\mathbf{y},t}\ \varphi_{\mathbf{z},t}]^T$ (yaw, pitch and roll angles respectively), and hence the propagation of the tip's position and orientation is described by Eqs. (16) and (17).

$$\mathbf{p}_{t+1} = \mathbf{p}_t + \mathbf{R}_t \mathbf{p}_{\Delta l},$$
$$\mathbf{R}_t = e^{(\varphi_{z,t}\mathbf{e}_3)^\wedge} e^{(\varphi_{y,t}\mathbf{e}_2)^\wedge} e^{(\varphi_{x,t}\mathbf{e}_1)^\wedge} \quad (16)$$
$$\mathbf{p}_{\Delta l} = r\begin{bmatrix}0 & \cos(\Delta l / r) - 1 & \sin(\Delta l / r)\end{bmatrix}^T$$
$$\mathbf{R}_{t+1} = \mathbf{R}_t e^{\Delta l / r (\mathbf{e}_1)^\wedge} \quad (17)$$

Where Δl is the insertion length during the time interval.

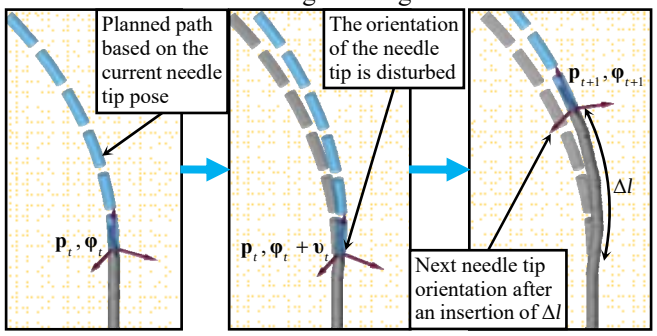

Fig. 6. The process of the needle deviating from its prescribed path due to disturbances on the needle tip

The uncertain motion of the needle is modeled as a steering process with the needle tip's orientation being constantly disturbed, as illustrated in Fig. 6. The needle tip orientation $\boldsymbol{\varphi}_t$ is then regarded as the unknown state variables and its position $\mathbf{p}_t$ is regarded as the output measured from the imaging modality. The state-space representation is summarized as follows.

$$\boldsymbol{\varphi}_{t+1} = \boldsymbol{\varphi}_t + \begin{bmatrix}\Delta l / r & 0 & 0\end{bmatrix}^T + \boldsymbol{\upsilon}_t \quad (18)$$
$$\mathbf{p}_{t+1} = h(\boldsymbol{\varphi}_t, \mathbf{p}_t) + \boldsymbol{\mu}_t \quad (19)$$

Where $h(\boldsymbol{\varphi}_t, \mathbf{p}_t)$ is the output model described in Eq. (16); $\boldsymbol{\upsilon}_t$ and $\boldsymbol{\mu}_t$ are process and observation noises with zero-mean Gaussian distribution with covariances $\mathbf{Q}_{prc}$ and $\mathbf{Q}_{obs}$.

The extended Kalman filter is given by Eq. (20) – (24).

- *Time update:*

$$\hat{\boldsymbol{\varphi}}_{t+1|t} = \hat{\boldsymbol{\varphi}}_{t|t} \quad (20)$$
$$\mathbf{P}_{t+1|t} = \mathbf{P}_{t|t} + \mathbf{Q}_{prc} \quad (21)$$

- *Measurement update*

$$\hat{\boldsymbol{\varphi}}_{t+1|t+1} = \hat{\boldsymbol{\varphi}}_{t+1|t} + \mathbf{K}_t \left(\mathbf{p}_{obs,t} - h(\hat{\boldsymbol{\varphi}}_{t+1|t}, \mathbf{p}_t)\right) \quad (22)$$
$$\mathbf{K}_t = \mathbf{P}_{t+1|t}\mathbf{H}_t^T \left(\mathbf{H}_t \mathbf{P}_{t+1|t} \mathbf{H}_t^T + \mathbf{Q}_{obs}\right)^{-1} \quad (23)$$
$$\mathbf{P}_{t+1|t+1} = \left(\mathbf{I} - \mathbf{K}_t \mathbf{H}_t\right)\mathbf{P}_{t+1|t} \quad (24)$$

Where $\mathbf{p}_{obs,t}$ is the observed needle tip position; $\mathbf{K}_t$ is the Kalman gain; $\mathbf{H}_t$ is the gradient of h.

$$\mathbf{H}_t = \frac{\partial h(\boldsymbol{\varphi}, \mathbf{p}_t)}{\partial \boldsymbol{\varphi}}\Big|_{\boldsymbol{\varphi}=\hat{\boldsymbol{\varphi}}_{t+1|t}}$$
$$= -e^{(\varphi_z \mathbf{e}_3)^\wedge} e^{(\varphi_y \mathbf{e}_2)^\wedge} e^{(\varphi_x \mathbf{e}_1)^\wedge} (\mathbf{p}_{\Delta l})^\wedge \begin{bmatrix}\mathbf{e}_1^T \\ \mathbf{e}_2^T e^{(\varphi_x \mathbf{e}_1)^\wedge} \\ \mathbf{e}_3^T e^{(\varphi_x \mathbf{e}_1)^\wedge} e^{(\varphi_y \mathbf{e}_2)^\wedge}\end{bmatrix}^T \Big|_{\boldsymbol{\varphi}=\hat{\boldsymbol{\varphi}}_{t+1|t}} \quad (25)$$

Once the estimation angles $\hat{\boldsymbol{\varphi}}$ are obtained, the needle tip's pose is readily obtained from Eq. (16) – (17), and the path re-planning is performed based on this estimation.

V. Experiment Validation

To validate the needle's steerability as well as the proposed kinematics model, a set of experiments were conducted.

A. Experimental Setup

Referring to Fig. 7, the needle insertion system is composed of three parts: the needle instrument carried by a linear and rotational module, the tissue simulant set beneath a camera, and a laptop as a central controller.

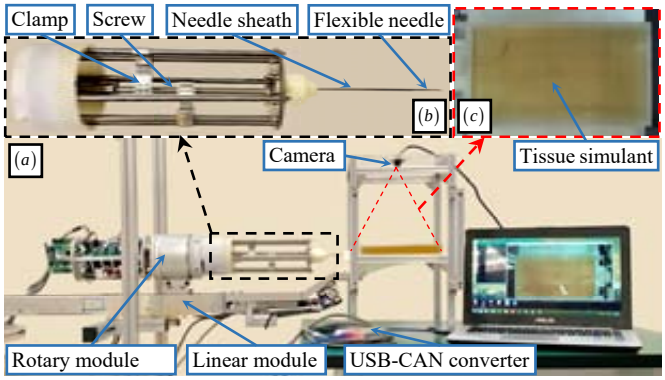

Fig. 7. Setup overview: (a) components of the needle insertion system; (b) the needle instrument, and (c) a camera view of the needle and tissue simulant.

The instrument is equipped with a needle sheath that aligns concentrically with the needle. The sheath is a customized stainless-steel tube fixed to the instrument, providing a straight passage toward the target tissue. A 3-D printed clamp connects the needle to the nut of a screw. The insertion of the needle along the sheath is driven by the screw, and the rotation of the needle about its axis is provided by the rotational module. The linear module is used to introduce the needle sheath into the tissue. The screw and the module are actuated by three Maxon motors that are controlled by 3 Maxon EPOS2 controllers.

A frame carrying the simulant tissues is set in front of the linear module, providing an insertion port for the needle sheath. A digital camera (USBFHD01M from Rervision Inc, China) is mounted on the top of the frame and is connected to the laptop to provide 2D image feedback of the needle in the tissue. The laptop (with 2.60GHz Intel Core i7-4510U CPU and 8G RAM) communicates with the EPOS through CAN bus. The path planning, needle state estimation and the required imaging process are all running on the laptop within the Matlab environment.

In the following experiments, the needle was assumed to steer in the plane normal to optical axis of the camera. The intrinsic parameters of the camera were obtained by camera calibration using the method in [25], and the mapping of the pixels in the camera to the points in the steering plane was obtained using a graph paper.

B. Steerability Test

To verify the effectiveness of the design discussed in Section III, the actual bending curvatures were tested in the tissue simulant.

Gel with different stiffness was cured to simulate different tissues. The gelatin-powder-to-water mass ratio was varied from 10% to 19%.

Eighteen insertions were performed for each needle-tissue pair. In each time, the needles were first introduced into the tissue by the sheath and then were inserted for a length of 40 mm without changing the bevel direction. The insertion speed was 1 mm/s. The insertion locations on the simulant were set different each time to avoid intersections of the paths of different insertions.

The final shapes of the needles were pictured by the camera. Pixels that didn't belong to the needle were manually removed. The radius of curvature was found then by fitting the pixels to a circle. The results are shown in Fig. 8. For the 10%, 13%, 16% and 19% gel, the mean radii of curvatures are 28.34 mm, 27.71 mm, 27.36 mm and 27.13 mm (an average of 27.6 mm), and the standard deviations are 0.247 mm, 0.237 mm, 0.459 mm and 0.473 mm, respectively. The results are considered close to the design goal of 30 mm curvature radius.

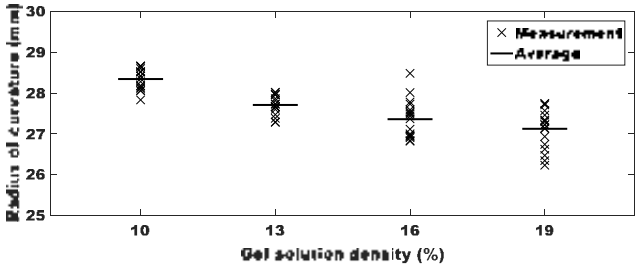

Fig. 8. Needle steerability test in gel solutions with different densities

C. Needle Insertion Experiment

Planar needle insertions with two known obstacles were carried out to validate the presented path planning and needle tip pose estimation algorithms. In the presented planar case, the needle path is composed of a few arcs that two adjacent ones have opposite steering directions. The path planning is hence performed with either $\delta_i = i\pi$ or $\delta_i = (i-1)\pi$. Also, the disturbances on the needle tip's orientation in off-plane directions φ_z and φ_y were ignored during the needle tip pose estimation.

The experimental process is shown in Fig. 9 and multi-media extension. The needle was first introduced into the tissue through the sheath, and started insertion after the path planning is completed. During the insertion, the needle tip was detected by matching the image from the camera to a template using normalized cross-correlation. The tip pose was then recursively estimated, and new paths were planned based on the estimation, after the insertion of a fixed length (20 mm in the experiments). Although the needle's actual path deviated from the planned path, the re-planning algorithm generated currently feasible paths and the target was reached with a 2-mm positioning accuracy over the 100-mm reach.

The experiments were repeated several times and similar results were mostly observed. Occasional insertion failures were due to the fact that the needle path re-planning was only performed every 20 mm insertion. The re-planning algorithm does not guarantee reaching success or obstacle avoidance, especially when the needle's tip is close to the target with a relatively large deviation from the planned path.

VI. Conclusion and Future Work

This paper proposes a novel needle design with passive tip articulation for increased steering curvature and reduced inter-tissue steerability variations. The working principle, the manufacturing-oriented needle design, the kinematics-based path planning with obstacle avoidance, the EKF-based needle tip pose estimation for path re-planning, and the experimental characterizations are reported in detail.

The proposed needle is shown to achieve tight and consistent path curvature (an average radius of curvature of 27.6 mm) in different tissue simulants. It can also reach a target deep inside the tissue simulant while avoiding obstacles. The needle may be promising for percutaneous applications.

Future work mainly includes conducting 3D *ex vivo* steering experiments to verify the validity of the kinematics model and the path planning algorithm. Shape sensing techniques (e.g., fiber Bragg grating) or other imaging modalities shall be incorporated to identify the needle path deviations, since the visual feedback in the 3D case will be difficult. A further investigation of the needle path deviation will be carried out, examining the deviations while varying the angle between the tip bevel plane and the direction of the first passive articulation joint, in order to improve the accuracy of the needle kinematics model.

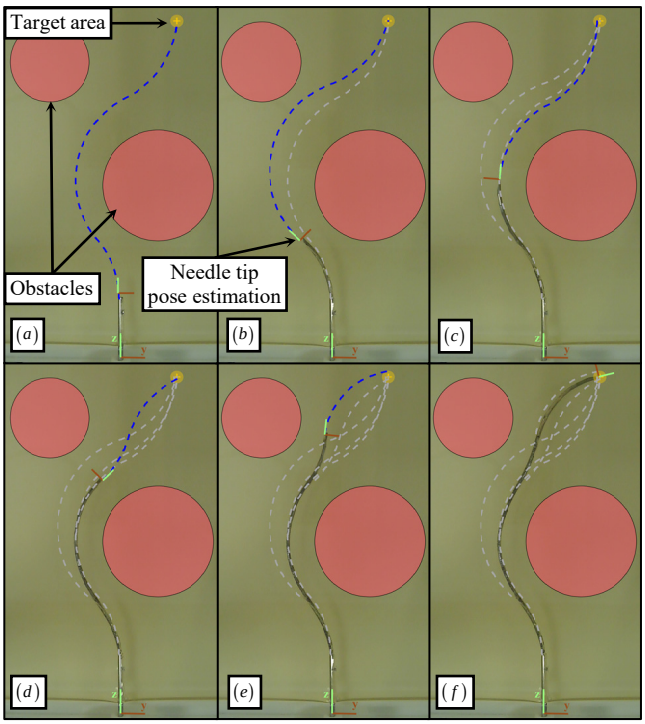

Fig. 9. Experimental process of path planning, needle insertion and tip pose estimation. The dashed blue and gray lines represent the current planned path and former planned paths respectively.

References

[1] N. J. Cowan, K. Goldberg, G. S. Chirikjian, G. Fichtinger, R. Alterovitz, K. B. Reed, V. Kallem, W. Park, S. Misra, and A. M. Okamura, "Robotic Needle Steering: Design, Modeling, Planning, and Image Guidance," in *Surgical Robotics: Systems Applications and Visions*, J. Rosen, B. Hannaford, and R. M. Satava, Eds.: Springer, 2011, pp. 557-581.

[2] N. J. van de Berg, D. J. van Gerwen, J. Dankelman, and J. J. van den Dobbelsteen, "Design Choices in Needle Steering—A Review," *IEEE/ASME Transactions on Mechatronics,* Vol. 20, No.5, pp. 2172-2183, Oct. 2015.

[3] S. P. DiMaio and S. E. Salcudean, "Needle Steering and Motion Planning in Soft Tissues," *IEEE Transactions on Biomedical Engineering,* Vol. 52, No.6, pp. 965-974, June 2005.

[4] D. Glozman and M. Shoham, "Image-Guided Robotic Flexible Needle Steering," *IEEE Transactions on Robotics,* Vol. 23, No.3, pp. 459-467, June 2007.

[5] Y. Adagolodjo, L. Goffin, M. d. Mathelin, and H. Courtecuisse, "Inverse Real-Time Finite Element Simulation for Robotic Control of Flexible Needle Insertion in Deformable Tissues," in *IEEE/RSJ International Conference on Intelligent Robots and Systems (IROS)*, Daejeon, Korea, 2016, pp. 2717-2722.

[6] R. J. Webster, J. S. Kim, N. J. Cowan, G. S. Chirikjian, and A. M. Okamura, "Nonholonomic Modeling of Needle Steering," *The International Journal of Robotics Research,* Vol. 25, No.5-6, pp. 509-525, May 2006.

[7] P. J. Swaney, J. Burgner, H. B. Gilbert, and R. J. Webster III, "A Flexure-Based Steerable Needle: High Curvature with Reduced Tissue Damage," *IEEE Transactions on Biomedical Engineering,* Vol. 60, No.4, pp. 906-909, April 2013.

[8] R. J. Roesthuis, N. J. van de Berg, J. J. van den Dobbelsteen, and S. Misra, "Modeling and Steering of a Novel Actuated-Tip Needle through a Soft-Tissue Simulant using Fiber Bragg Grating Sensors," in *IEEE International Conference on Robotics and Automation (ICRA)*, Seattle, WA, USA, 2015, pp. 2283-2289.

[9] G. Gerboni, J. D. Greer, P. F. Laeseke, G. L. Hwang, and A. M. Okamura, "Highly Articulated Robotic Needle Achieves Distributed Ablation of Liver Tissue," *IEEE Robotics and Automation Letters,* Vol. 2, No.3, pp. 1367-1374, July 2017.

[10] P. Sears and P. Dupont, "A Steerable Needle Technology Using Curved Concentric Tubes," in *IEEE/RSJ International Conference on Intelligent Robots and Systems (IROS)*, Beijing, China, 2006, pp. 2850-2856.

[11] R. J. Webster, A. M. Okamura, and N. J. Cowan, "Toward Active Cannulas: Miniature Snake-Like Surgical Robots," in *IEEE/RSJ International Conference on Intelligent Robots and Systems (IROS)*, Beijing, China, 2006, pp. 2857-2863.

[12] P. E. Dupont, J. Lock, B. Itkowitz, and E. Butler, "Design and Control of Concentric-Tube Robots," *IEEE Transactions on Robotics,* Vol. 26, No.2, pp. 209-225, April 2010.

[13] H. B. Gilbert, J. Neimat, and R. J. Webster III, "Concentric Tube Robots as Steerable Needles: Achieving Follow-the-Leader Deployment," *IEEE Transactions on Robotics,* Vol. 31, No.2, pp. 246-258, Apr. 2015.

[14] D. Glozman and M. Shoham, "Flexible Needle Steering and Optimal Trajectory Planning for Percutaneous Therapies " in *International Conference on Medical Image Computing and Computer-Assisted Intervention (MICCAI)*, Saint Malo, France, 2004, pp. 137-144.

[15] M. Khadem, C. Rossa, N. Usmani, R. S. Sloboda, and M. Tavakoli, "Robotic-Assisted Needle Steering Around Anatomical Obstacles using Notched Steerable Needles," *IEEE Journal of Biomedical and Health Informatics,* Vol. 22, No.6, pp. 1917-1928, Nov. 2018.

[16] T. R. Wedlick and A. M. Okamura, "Characterization of Pre-Curved Needles for Steering in Tissue," in *International Conference of the IEEE Engineering in Medicine and Biology Society (EMBC)*, Minneapolis, MN, USA, 2009, pp. 1200-1203.

[17] T. K. Adebar, J. D. Greer, P. F. Laeseke, G. L. Hwang, and A. M. Okamura, "Methods for Improving the Curvature of Steerable Needles in Biological Tissue," *IEEE Transactions on Biomedical Engineering,* Vol. 63, No.6, pp. 1167-1177, June 2016.

[18] S. Pattanshetti, R. Sandström, A. Kottala, N. M. Amato, and S. C. Ryu, "Feasibility Study of Robotic Needles with a Rotational Tip-Joint and Notch Pattern," in *IEEE International Conference on Robotics and Automation (ICRA)*, Montreal, Canada, 2019, pp. 1534-1540.

[19] S. Misra, K. B. Reed, B. W. Schafer, K. T. Ramesh, and A. M. Okamura, "Mechanics of Flexible Needles Robotically Steered through Soft Tissue," *The International Journal of Robotics Research,* Vol. 29, No.13, pp. 1640-1660, June 2010.

[20] R. J. Roesthuis, Y. R. J. v. Veen, A. Jahya, and S. Misra, "Mechanics of Needle-Tissue Interaction," in *IEEE/RSJ International Conference on Intelligent Robots and Systems (IROS)*, San Francisco, CA, USA, 2011, pp. 2557-2563.

[21] R. Alterovitz, M. Branicky, and K. Goldberg, "Motion Planning Under Uncertainty for Image-guided Medical Needle Steering," *International Journal of Robotics Research,* Vol. 27, No.11-12, pp. 1361-1374, 2008.

[22] S. Patil, J. Burgner, R. J. Webster III, and R. Alterovitz, "Needle Steering in 3-D via Rapid Replanning," *IEEE Transactions on Robotics,* Vol. 30, No.4, pp. 853-864, Aug. 2014.

[23] V. Duindam, J. Xu, R. Alterovitz, S. Sastry, and K. Goldberg, "Three-Dimensional Motion Planning Algorithms for Steerable Needles Using Inverse Kinematics," *The International Journal of Robotics Research,* Vol. 29, No.7, pp. 789-800, Oct. 2009.

[24] D. E. Whitney, "Resolved Motion Rate Control of Manipulators and Human Prostheses," *IEEE Transactions on Man-Machine Systems,* Vol. 10, No.2, pp. 47-53, June 1969.

[25] Z. Zhang, "Flexible Camera Calibration by Viewing a Plane from Unknown Orientations," in *IEEE International Conference on Computer Vision (ICCV)*, Kerkyra, 1999, pp. 666-673.